Disruption of Adaptive Immunity Enhances Disease in SARS-CoV-2-Infected Syrian Hamsters

Rebecca L. Brocato,[a] Lucia M. Principe,[a] Robert K. Kim,[b] Xiankun Zeng,[b] Janice A. Williams,[b] Yanan Liu,[c] Rong Li,[c] Jeffrey M. Smith,[a] Joseph W. Golden,[a] Dave Gangemi,[d,e] Sawsan Youssef,[d,e] Zhongde Wang,[c] Jacob Glanville,[d,e] Jay W. Hooper[a]

[a]Virology Division, United States Army Research Institute of Infectious Diseases, Frederick, Maryland, USA
[b]Pathology Division, United States Army Research Institute of Infectious Diseases, Frederick, Maryland, USA
[c]Department of Animal, Dairy and Veterinary Sciences, Utah State University, Logan, Utah, USA
[d]Distributed Bio, Inc., South San Francisco, California, USA
[e]Centivax, Inc., South San Francisco, California, USA

ABSTRACT Animal models recapitulating human COVID-19 disease, especially severe disease, are urgently needed to understand pathogenesis and to evaluate candidate vaccines and therapeutics. Here, we develop novel severe-disease animal models for COVID-19 involving disruption of adaptive immunity in Syrian hamsters. Cyclophosphamide (CyP) immunosuppressed or *RAG2* knockout (KO) hamsters were exposed to severe acute respiratory syndrome coronavirus 2 (SARS-CoV-2) by the respiratory route. Both the CyP-treated and *RAG2* KO hamsters developed clinical signs of disease that were more severe than those in immunocompetent hamsters, notably weight loss, viral loads, and fatality (*RAG2* KO only). Disease was prolonged in transiently immunosuppressed hamsters and was uniformly lethal in *RAG2* KO hamsters. We evaluated the protective efficacy of a neutralizing monoclonal antibody and found that pretreatment, even in immunosuppressed animals, limited infection. Our results suggest that functional B and/or T cells are not only important for the clearance of SARS-CoV-2 but also play an early role in protection from acute disease.

IMPORTANCE Syrian hamsters are in use as a model of disease caused by SARS-CoV-2. Pathology is pronounced in the upper and lower respiratory tract, and disease signs and endpoints include weight loss and viral RNA and/or infectious virus in swabs and organs (e.g., lungs). However, a high dose of virus is needed to produce disease, and the disease resolves rapidly. Here, we demonstrate that immunosuppressed hamsters are susceptible to low doses of virus and develop more severe and prolonged disease. We demonstrate the efficacy of a novel neutralizing monoclonal antibody using the cyclophosphamide transient suppression model. Furthermore, we demonstrate that *RAG2* knockout hamsters develop severe/fatal disease when exposed to SARS-CoV-2. These immunosuppressed hamster models provide researchers with new tools for evaluating therapies and vaccines and understanding COVID-19 pathogenesis.

KEYWORDS COVID-19, SARS-CoV-2, Syrian hamster, animal models, cyclophosphamide, disease, monoclonal antibody

The ongoing pandemic has led to the search for animal models that faithfully recapitulate salient features of human coronavirus disease (COVID-19) for pathogenesis studies and evaluation of vaccines and therapeutics (1). Early reports indicated that Syrian hamsters, whose ACE2 is highly homologous to its human ortholog, were highly susceptible to severe acute respiratory syndrome coronavirus 2 (SARS-CoV-2) infection but did not develop severe disease (2, 3). In 2008, administration of cyclo-
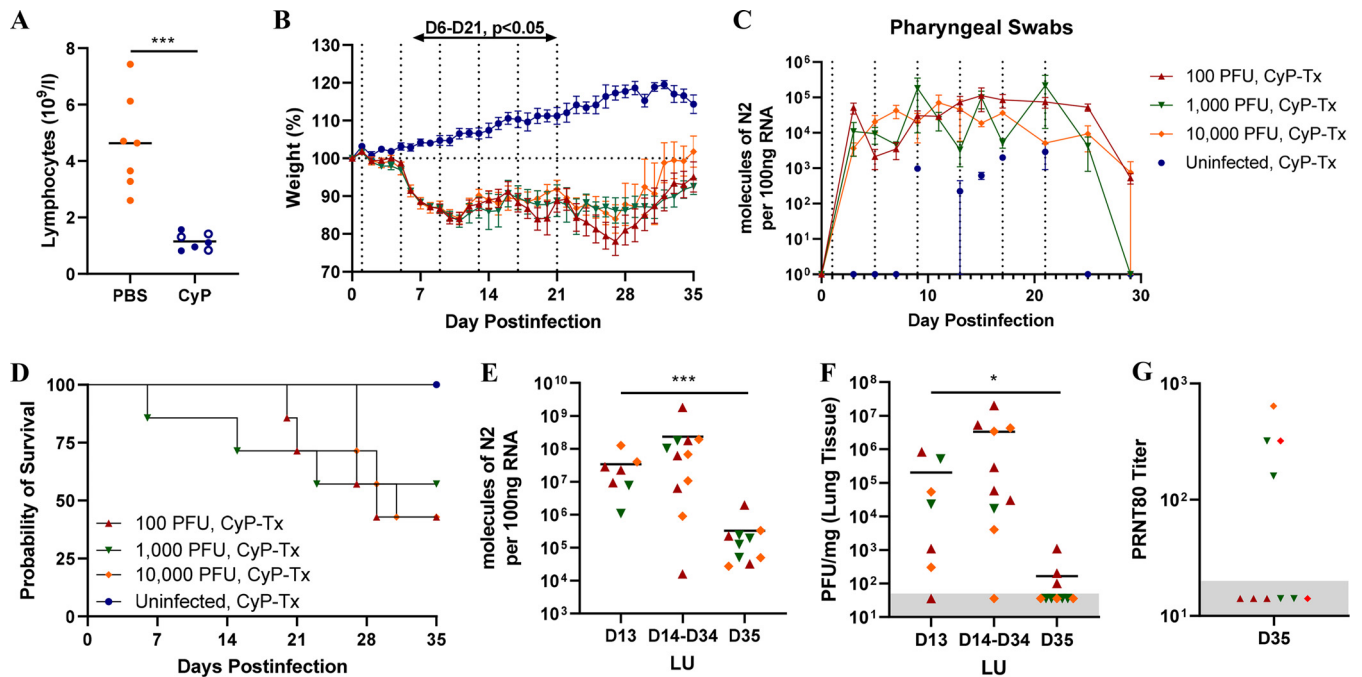
FIG 1 CyP-treated, SARS-CoV-2-infected hamsters. Groups of 10 Syrian hamsters each were immunosuppressed with CyP. (A) Lymphocyte counts were determined from whole blood 3 days (closed symbols) or 4 days (open symbols) following the CyP loading dose. Hamsters were exposed to increasing doses of SARS-CoV-2 intranasally on day 0. (B) Weights were monitored for 35 days. (C) Viral RNA copies per pharyngeal swab were assayed at the indicated times postinfection. CyP administration is depicted by vertical dotted lines in panels B and C. Hamsters were monitored for (D) survival, and lung tissue collected either at the time of death or scheduled euthanasia 13 or 35 dpi was assessed for viral load by (E) Reverse transcription-PCR (RT-PCR) and (F) plaque assay. (G) Blood was collected from surviving hamsters at 35 dpi and assessed by plaque reduction or neutralization test. LU, lung.

phosphamide (CyP), an alkylating agent that suppresses B-cell and T-cell function, was used to develop a severe-disease model for SARS-CoV in Syrian hamsters (4). We reasoned that a similar approach might allow the development of a severe-disease model for SARS-CoV-2. Moreover, clinical findings of lymphopenia associated with COVID-19 (5) and its prominence in severe cases (6, 7) suggested that an immunosuppressed animal model of COVID-19 might more accurately model some aspects of severe human disease. Here, we used CyP-treated and *RAG2* knockout (KO) hamsters to investigate how transient disruption, or ablation, of the adaptive immune response affects SARS-CoV-2 infection. In addition, we used the immunocompetent and immunosuppressed hamster models to evaluate whether preexposure to virus through previous infection or exposure to neutralizing antibodies was sufficient to limit or prevent disease.

RESULTS

Transient immunosuppression using CyP increased the duration and severity of disease in SARS-CoV-2-infected hamsters. In our first experiment manipulating the adaptive immune response, we immunosuppressed hamsters using CyP (CyP-Tx) beginning at −3 days postinfection (dpi). Suppression of lymphocytes was confirmed by hematology analysis just prior to challenge (Fig. 1A). On day 0, groups of 10 hamsters were exposed to 100, 1,000, or 10,000 PFU of SARS-CoV-2 by the intranasal route. Disease progression was monitored by weight loss (Fig. 1B) and detection of viral RNA in pharyngeal swabs using reverse transcription-PCR (RT-PCR) (Fig. 1C). Weight loss was remarkably similar between all SARS-CoV-2-exposed groups regardless of dose, with drastic weight loss beginning 6 dpi. Weight loss remained significant relative to starting weight through 35 dpi. In contrast, mock (phosphate-buffered saline [PBS])-challenged hamsters treated with CyP steadily gained weight, with a few exceptions. Specifically, one cage of four mock-challenged hamsters showed evidence of weight loss 9 to

12 dpi. These same animals were the only mock-challenged hamsters that were positive starting at 9 dpi in the SARS-CoV-2 pharyngeal swab RT-PCR analysis (Fig. 1C).

All of the SARS-CoV-2-challenged hamsters had detectable viral RNA in pharyngeal swabs at the first time point assayed, 3 dpi, and remained consistent (10^3 to 10^5 molecules of nucleocapsid using a second primer set [N2] per 100 ng RNA) throughout the duration of CyP treatment (Fig. 1C). After the last CyP treatment at 21 dpi, most of the hamsters continued to lose weight, and several hamsters began to exhibit signs of a wasting disease, i.e., cachexia and extreme weight loss, requiring euthanasia (Fig. 1B and D). Then, approximately 7 days after cessation of CyP, the remaining hamsters started gaining weight, and viral RNA levels in pharyngeal swabs dropped below 10^3 molecules of N2 per 100 ng RNA (Fig. 1C). Viral RNA and infectious virus were detected in lung tissue from a subset of hamsters collected 13 dpi, on the day of euthanasia of moribund animals (14 to 34 dpi), or after euthanasia at 35 dpi (end of study) (Fig. 1E and F). There was a statistically significant reduction in lung viral burden comparing lung homogenates from 35 dpi to those from 13 dpi. Serum collected from surviving hamsters at 35 dpi was assayed for neutralizing antibodies (Fig. 1G). Six of the 10 infected hamsters that survived in the CyP immunosuppression experiment never developed detectable levels of neutralizing antibodies. Interestingly, the four hamsters that did develop neutralizing antibodies after CyP treatment cessation rebounded more rapidly as measured by weight gain (data not shown). Together, these data indicate that CyP treatment allowed a persistent infection that was reversed in most animals when CyP treatment was stopped and the adaptive immune response was allowed to recover.

RAG2 KO hamster infection with SARS-CoV-2 results in a lethal model. _RAG2_ KO hamsters deficient in recombination activation gene 2 do not produce functional T or B cells (8). Whereas CyP treatment allowed transient and partial immunosuppression, the _RAG2_ KO hamsters allowed us to evaluate the outcome of SARS-CoV-2 infection in the absence of functional lymphocytes. _RAG2_ KO hamsters were exposed to 10,000 PFU SARS-CoV-2 by the intranasal route. The _RAG2_ KO hamsters showed significant weight loss starting at 3 dpi (Fig. 2A), and the infection was uniformly lethal, with a median day-to-death of 6 days ($P = 0.0025$; log rank test) (Fig. 2B). Viral RNA amounts detected from pharyngeal swabs trended to be higher than in those from the CyP-treated hamsters, but this was not statistically significant (Fig. 2C). The 10,000 PFU and PBS mock groups from the CyP experiment shown in Fig. 1 were included in Fig. 2A to C for comparison. Organs from the _RAG2_ KO animals that succumbed or met euthanasia criteria were homogenized and evaluated for viral RNA by RT-PCR. Viral RNA was present at the highest levels in the lung and trachea. Lower levels of viral RNA were also detected in extrapulmonary organs, including the heart, liver, spleen, intestine, brain, and kidney (Fig. 2D).

Increased pathology of SARS-CoV-2-infected _RAG2_ KO hamsters includes hemorrhage and severe edema. A subset of the SARS-CoV-2-infected hamsters from the CyP experiment shown in Fig. 1 were euthanized at 13 dpi. Lungs were formalin fixed, paraffin embedded, and evaluated by histopathology and _in situ_ hybridization (ISH) (Fig. 3). Lung tissue from necropsied animals demonstrated focally extensive areas consolidation of pulmonary parenchyma admixed with dense aggregates of inflammatory cells (Fig. 3A). The bronchial lumina are multifocally lined by hyperplastic respiratory epithelium (Fig. 3B), and SARS-CoV-2 genomic RNA was frequently detected by ISH in alveolar pneumocytes, alveolar infiltrates, and bronchiolar epithelial cells (Fig. 3C). At 14 dpi, immunocompetent hamsters infected with SARS-CoV-2 exhibited only mild congestion and inflammatory infiltration, indicating recovery from viral challenge (2) and supporting the hypothesis that CyP administration to disrupt adaptive immunity exacerbates and prolongs disease in hamsters.

Lung tissue collected at the time of death of SARS-CoV-2-infected _RAG2_ KO hamsters contain areas of hemorrhage and inflammation expanding the interstitium and connective tissue surrounding bronchi and arteries (Fig. 3D). As seen in the CyP-treated hamsters, the bronchial lumina of _RAG2_ KO hamsters is lined with multiple layers of
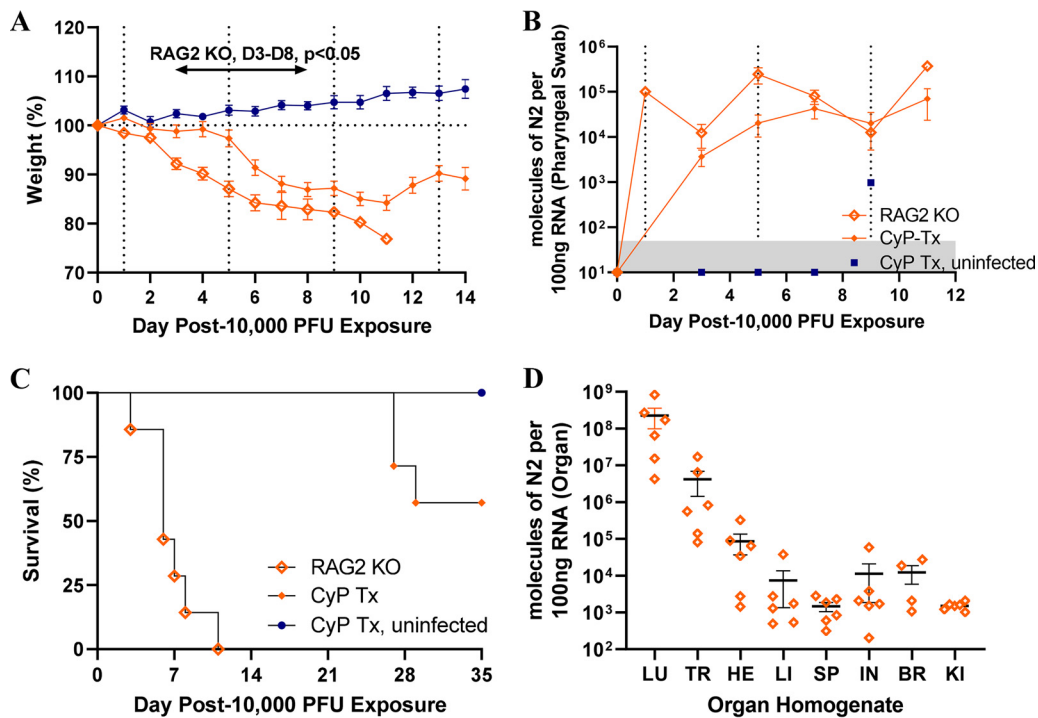
FIG 2 SARS-CoV-2-infected *RAG2* knockout (KO) hamsters. Either *RAG2* KO (*n* = 7) or CyP-treated hamsters (*n* = 10, from Fig. 1) were exposed to 10,000 PFU SARS-CoV-2 on day 0. Vertical dotted lines (A, B) indicate CyP treatment for indicated animals. Hamsters were monitored for (A) weight and (C) survival. (B) Viral RNA copies per pharyngeal swab were assayed at the indicated times postinfection. (D) Organs collected at the time of death were homogenized and assayed for viral load. LU, lung; TR, trachea; HE, heart; LI, liver; SP, spleen; IN, intestine; BR, brain; KI, kidney.

infected epithelial and club cells, which contain infiltrates of lymphocytes (presumably nonfunctional), heterophils, and macrophages (Fig. 3E, G and H). There is hemorrhage within the alveolar lumen and consolidation with septal congestion. Also, as observed in CyP-treated hamsters, SARS-CoV-2 genomic RNA and viral antigen were frequently detected in alveolar pneumocytes (Fig. 3I), alveolar infiltrates, and bronchiolar epithelial cells (Fig. 3F). Together, these data indicate that the absence of functional B and T cells in *RAG2* KO hamsters allows increased pathology and lethality from SARS-CoV-2 infection.

Electron microscopy studies were performed on lung sections of SARS-CoV-2-infected, CyP-treated hamsters with various lung viral loads (Fig. 1). The lungs lack a typical morphology in which a distinct interalveolar septum with capillaries and type I and type II pneumocytes is clearly evident. The animal with the lowest viral load (10^6 molecules of N2 per 100 ng RNA, Fig. 3J) showed some remnants of normal architecture, while the animal with the highest viral load (10^8 molecules of N2 per 100 ng RNA, Fig. 3L) lacked the prominent alveolar space and were congested with immune cells. The lamellar bodies in the type II pneumocytes are still identifiable in hamsters with high viral loads.

The SARS-CoV-2 virion is reported to range in diameter from 50 to 160 nm (with surface spikes measuring approximately 20 nm) (9–13). The low- and high-viral-load samples show compartmentalized vacuoles with round virus-like structure and vesicles with irregular shaped structures resembling multivesicular bodies (Fig. 3J to L). The more electron-dense vesicles are suggestive of mature virus particles, whereas the less electron-dense particles are likely immature virions. In addition to cytoplasmic vacuoles, these tissues show swollen rough endoplasmic reticulum (rER) (Fig. 3L). Swollen rER appears as a result of cellular stress and/or increased viral protein synthesis. Immuno-gold labeling is necessary to confirm the presence of virus particles.

Tracheas from the same SARS-CoV-2-infected, CyP-treated hamsters with various lung viral loads were analyzed by electron microscopy. These tracheas also exhibit
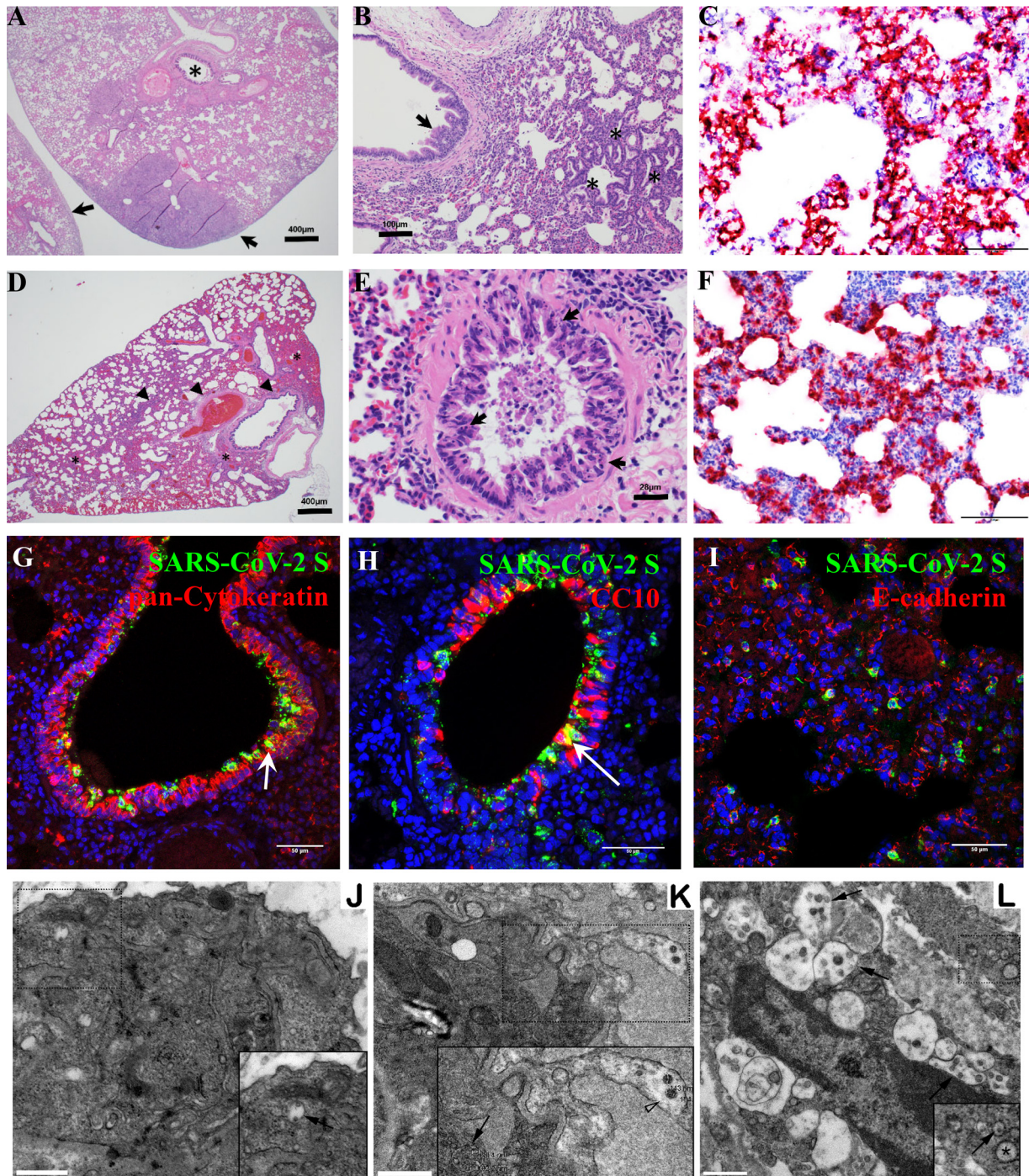
FIG 3 Pathology of SARS-CoV-2 in CyP-treated and *RAG2* KO hamsters. Hematoxylin and eosin (H&E) sections (A, B) of lung tissue from CyP-treated hamsters euthanized at 13 dpi show extensive areas of consolidation with dense aggregates of inflammatory cells. (A) Bronchial lumina are lined by hyperplastic folds of respiratory epithelium (asterisk) and the pleural surface is multifocally thickened and expanded by fibrous connective tissue and inflammatory cells (arrows). (B) The bronchial lumina are lined by hyperplastic folds of respiratory epithelium (arrow). Areas of alveolar septa lined rows of type 2 pneumocytes (asterisks). (C) SARS-CoV-2 genomic RNA was frequently detected by *in situ* hybridization (ISH) in alveolar pneumocytes, alveolar infiltrates, and bronchiolar respiratory epithelial cells from CyP-treated hamsters. H&E sections (D, E) of lung tissue from *RAG2* KO hamsters collected at the time of death. (D) Areas of hemorrhage (asterisk) and inflammation (arrowheads) expanding the interstitium and connective tissue surrounding the bronchi and arteries (arrows). (E) Necrotic bronchial epithelium (arrows) overlaid by hemorrhagic exudate. Peribronchial connective tissue is expanded by lymphocytes, heterophils (asterisks), and fewer macrophages that often contain hemosiderin (arrowheads). There is marked consolidation in surrounding alveoli with marked septal congestion and expansion by previously mentioned inflammatory cells. (F) SARS-CoV-2 genomic RNA was frequently detected by ISH in alveolar pneumocytes, alveolar infiltrates, and bronchiolar epithelial cells from *RAG2* KO hamsters. (G to I) Immunofluorescence assays demonstrate that SARS-CoV-2 antigens (S or NP, green) were detected in bronchiolar epithelium-labeled anti-pan-cytokeratin antibody (red) (G) club (Clara) cells labeled by anti-CC10 antibody (red) (H) and alveolar epithelial cells labeled by anti-E-cadherin antibody (red) (I) in *RAG2* KO hamsters. (J to L) Transmission electron microscopy of hamster lungs with
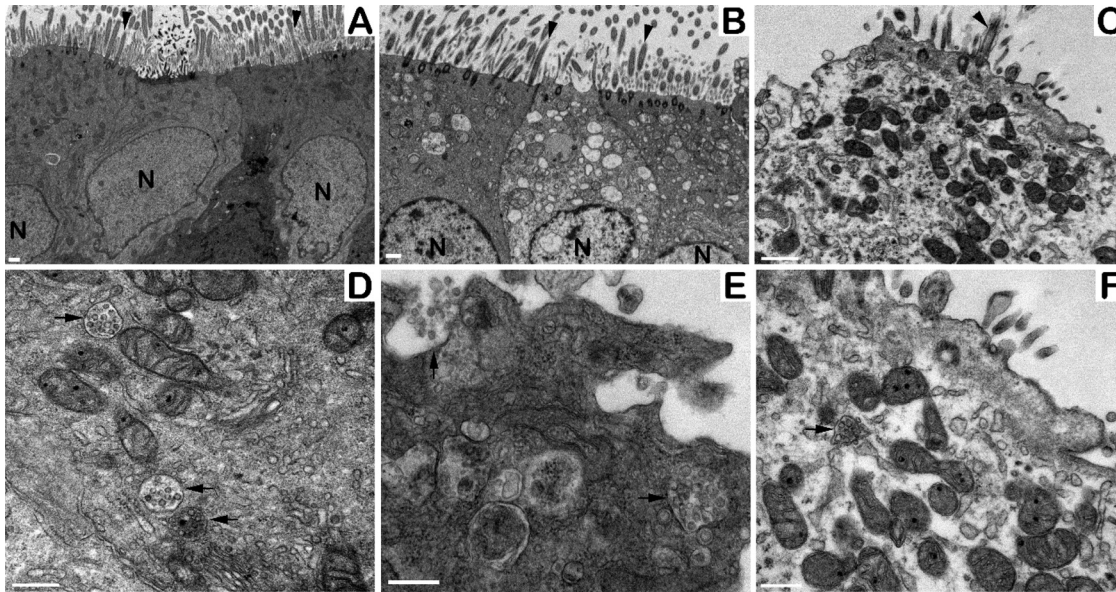
(Continued on next page)

FIG 4 SARS-CoV-2 disrupts the tracheal epithelial layer. Tracheal sections were collected from SARS-CoV-2-infected, CyP-treated hamsters, sorted by lung viral load and analyzed by transmission electron microscopy. (A) The animal with a lung viral load of 10^6 molecules of N2 per 100 ng of RNA showed the most intact ciliated cells on the surface of the trachea (arrowheads). As viral load increases (from animals with lung viral loads of 10^7 [B] and 10^8 [C] molecules of N2 per 100 ng RNA, respectively), the presence of ciliated cells and epithelial cells lining the tracheal lumen decreases. (D) Cells from the low-viral-load animal show several cytoplasmic vacuoles with potential immature viral particles (arrows). (E) Release of cytoplasmic vacuole content (possible immature virions, arrows) into the luminal space of a cell that has detached from the epithelial layer. (F) From the animal with the highest viral load, very few ciliated cells were noted. Cytoplasmic vacuole with potential immature viral particles (arrow). Bars are as follows: (A to C) 1 μm and (D to F) 500 nm.

disruption of the epithelial layer. Trachea from the animal with the lowest lung viral load (10^6 molecules of N2 per 100 ng RNA) showed mostly intact ciliated cells on the surface (Fig. 4A). These cells show several cytoplasmic vacuoles with potential immature virus particles (Fig. 4D and E). As the lung viral load increases, the presence of ciliated cells and epithelial cells lining the tracheal lumen decreases (Fig. 4B and C, respectively). Very few ciliated cells were seen in the animals with the heaviest viral load (10^8 molecules of N2 per 100 ng RNA), and there is an absence of cytoplasmic content that is marked by the lack of electron-dense cytoplasmic vesicles (Fig. 4F).

Protective efficacy of prior SARS-CoV-2 infection. Nine previously infected immunocompetent hamsters from two separate experiments were retained for a rechallenge with SARS-CoV-2. Our goal was to determine if prior infection elicited protective immunity. To ensure that these hamsters had cleared infectious virus after the initial challenge, hamsters were treated with 3 doses of CyP and weights were monitored for 14 days (Fig. 5A). If the animals were persistently infected, we predicted that hamsters would experience onset of disease following CyP administration, as measured by rapid weight loss and positive pharyngeal swab RT-PCR. No significant weight loss was detected, and swabs were negative for viral RNA (Fig. 5A). All nine animals were positive for neutralizing antibodies prior to the rechallenge (Fig. 5B). The nine previously exposed hamsters and seven naive hamsters were challenged with 100,000 PFU SARS-CoV-2. Weights were monitored daily, and pharyngeal swabs were collected every

FIG 3 Legend (Continued)

increasing viral loads. (J) Lung section from hamster with 10^6 molecules of N2 per 100 ng RNA. Inset shows cytoplasmic vacuole with possible virus (black arrow). (K) Lung section from hamster with 10^7 molecules of N2 per 100 ng RNA. Potential mature viral particles (approximately 143 to 154 nm in diameter, arrowhead) are present at the cell periphery, and suspected immature virions are detected more internally in a cytoplasmic vacuole (approximately 62 to 97 nm in diameter, black arrow). (L) Lung section from hamster with 10^8 molecules of N2 per 100 ng RNA. Numerous cytoplasmic vacuoles of possible virus are evident (black arrows). Inset shows an example of swollen rough endoplasmic reticulum (rER) (asterisk) with virus forming within the swollen rER (black arrow). Bars are as follows: (A, D) 400 μm, (B) 100 μm, (E) 28 μm, (C, F) 100 μm, (G, H, I) 50 μm, and (J-L) 1 μm.
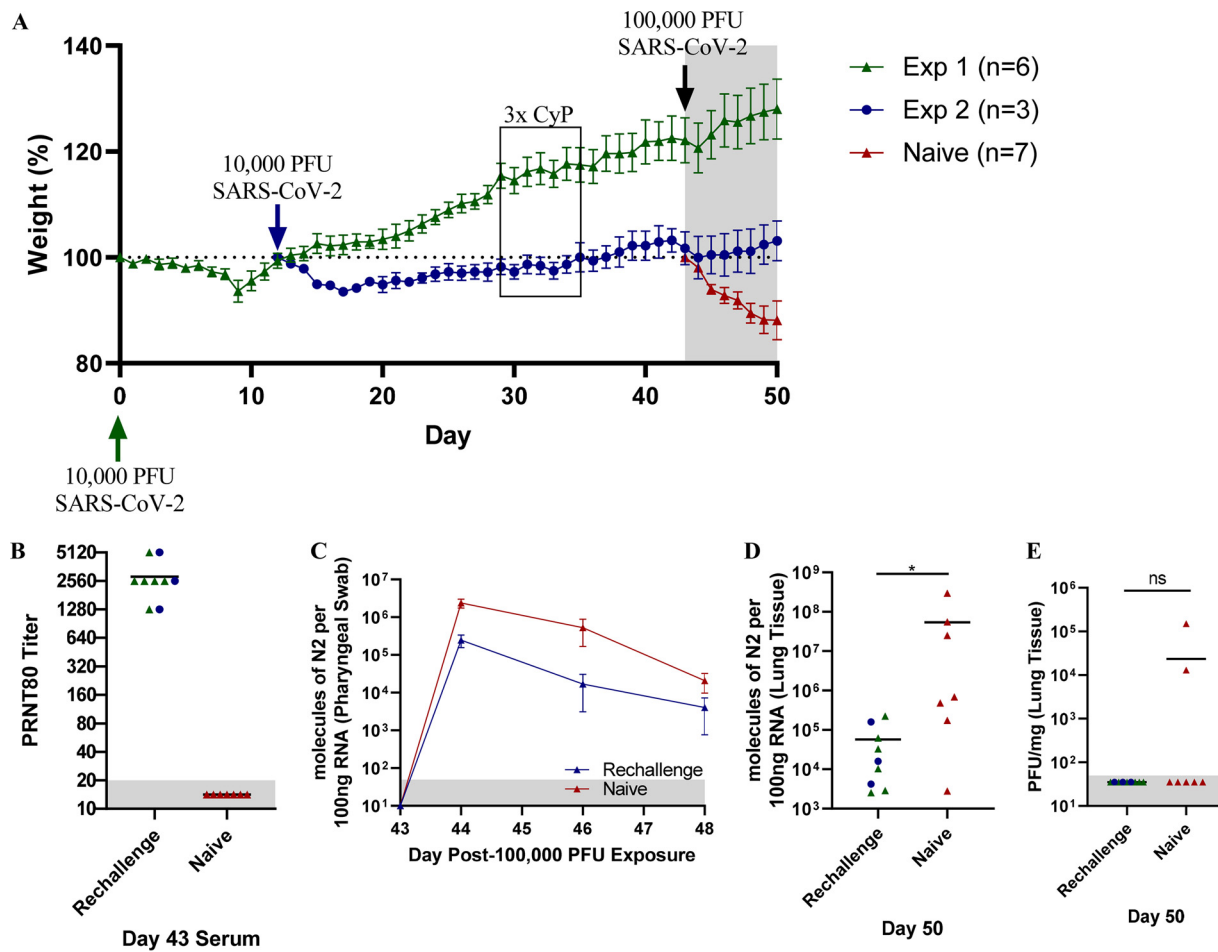
FIG 5 Rechallenge of previously infected SARS-CoV-2 hamsters. (A) Weight data from hamsters initially exposed to 10,000 PFU SARS-CoV-2 and rechallenged with 100,000 PFU SARS-CoV-2. (B) PRNT$_{80}$ titers depicting the level of circulating neutralizing antibody prior to virus exposure on day 43. Disease progression was monitored by (A) weight and (C) pharyngeal swabs. Lung tissue collected on day 50 was assayed for (D) viral RNA and (E) infectious virus.

other day for viral RNA RT-PCR. Control animals lost weight as predicted, whereas the previously exposed animals were protected from significant weight loss. Pharyngeal swab RT-PCR indicated a statistically significant reduction in viral RNA detected in rechallenged animals compared to that in naive animals (Fig. 5C). In addition, the viral load in lung homogenates from animals euthanized at the end of the study indicated a statistically significant ($P = 0.0164$; unpaired t test) reduction in viral RNA level in the rechallenged animals Fig. 5D). There was no infectious virus in the lungs of the rechallenged hamster 7 days after exposure. However, only two of the naive hamsters had infectious virus after challenge (Fig. 5E). The likely reason for the disappearance of infectious virus in the lungs of the naive group is that those animals had already mounted an immune response and infectious virus was cleared by the time the lung samples were collected. Together, these data indicate that immunocompetent hamsters that had recovered from prior exposure to SARS-CoV-2 were not persistently infected, but instead were protected (i.e., protective immunity).

Protective efficacy of anti-SARS-CoV-2 MAb. A human monoclonal antibody (MAb) targeting the spike protein of SARS-CoV-2 was evaluated in a passive transfer experiment using immunosuppressed hamsters. Centi-F1 MAb (30 mg/kg; 50% inhibitory concentration [IC$_{50}$] = 391 ng/ml and 80% plaque reduction/neutralization titer [PRNT$_{80}$] = 1,280), a control IgG (normal) MAb, or PBS were administered at −1 dpi. On day 0, the immunosuppressed animals were challenged with 1,000 PFU SARS-CoV-2. Neutralizing antibody levels in serum at the time of challenge were measured by

FIG 6 Passive transfer of anti-SARS-CoV-2 MAb Centi-F1 in immunosuppressed hamsters. Groups of 8 hamsters were immunosuppressed with CyP beginning at −3 dpi (indicated by the vertical lines in panels B and C), were passively transferred 30 mg/kg of Centi-F1 MAb, an equivalent volume of normal MAb, or PBS at −1 dpi, and were exposed to 1,000 PFU SARS-CoV-2 on day 0. (A) Levels of circulating neutralizing antibody from day 0 serum were assayed by PRNT. Disease progression was monitored by (B) weight and (C) pharyngeal swabs. Lung tissue collected at 13 dpi was assayed for (D) viral RNA and (E) infectious virus.

PRNT$_{80}$ (Fig. 6A). Detectable levels ranging from PRNT80 titers of 80 to ≥640 were found in the Centi-F1 MAb group. Disease progression was monitored by weight change (Fig. 6B) and pharyngeal swab RT-PCR (Fig. 6C). Hamsters administered the normal MAb or PBS exhibited significant weight loss starting at 5 dpi and ultimately had group weights drop to 86% and 91%, respectively. Hamsters treated with Centi-F1 MAb maintained over 100% of their day 0 weight to the conclusion of the experiment (13 dpi). Viral RNA was detected in pharyngeal swabs in all groups but trended lower in Centi-F1 MAb-treated animals on day 11 ($P = 0.1038$; unpaired t test). Similarly, lung tissue collected at 13 dpi (end of study) indicate comparable levels of viral RNA detected (Fig. 6D) but significantly reduced infectious virus in Centi-F1 MAb-treated animals ($P = 0.0002$; unpaired t test) (Fig. 6E). These findings demonstrate that a SARS-CoV-2 MAb can limit infection in immunosuppressed animals.

DISCUSSION

It has been postulated that both innate immune hyperactivity and adaptive immune dysfunction result in increased SARS-CoV-2 dissemination and drive severe disease (14). In order to develop a small animal model of severe disease, evaluate the role of adaptive immunity, and replicate the COVID-19 lymphopenia observed in human disease, we treated hamsters with CyP. In this immunosuppressed model, we observe more drastic weight loss, high levels of virus in the lung, and viral persistence that did not begin to resolve until CyP treatment was stopped (Fig. 1). Histopathologic findings in the lungs of CyP-treated hamsters also demonstrate prolonged pathology and ongoing repair through hyperplastic changes of the

bronchial epithelium and type II pneumocytes that were not observed in the sampled *RAG2* KO hamsters. These data demonstrate the critical role B and T cells play in resolution of disease and describe an animal model for severe COVID-19 disease that can be used for rigorous testing of medical countermeasures.

The recent development of immune function KO hamsters combined with Syrian hamster susceptibility to SARS-CoV-2 infection allows investigation of the role of specific immune functions in COVID-19 pathogenesis and protection. Thus far, *STAT2* KO hamsters have been used to demonstrate that type I interferon plays a role in restricting viral dissemination and promoting lung pathology in SARS-CoV-2-infected animals (15). Here, we found unexpectedly that SARS-CoV-2 challenge resulted in a uniform lethality in the *RAG2* KO hamsters. It is interesting that onset of disease, as measured by weight loss, was more rapid (by 3 days) in the *RAG2* KO animals than that in immunocompetent, or even transiently immunosuppressed, hamsters receiving the same challenge dose. This indicates that the absence of functional B cells and/or T cells exacerbates pathogenesis at a very early stage (within a day or two) after exposure to virus. The importance of T cells in viral clearance has been noted for other coronaviruses, namely SARS-CoV (16) and Middle East respiratory syndrome (MERS) (17). In fact, depletion of CD3$^+$ T cells correlates with severity and adverse outcomes (18).

There have been anecdotal accounts suggesting that immunity generated from an initial SARS-CoV-2 infection in humans may not be protective against a subsequent infection. Recent studies using nonhuman primates indicated that prior infection results in protective immunity (19). Here, we show that the immune response from an initial SARS-CoV-2 infection, including a robust neutralizing antibody response, is protective against rechallenge. We detected reduced levels of viral RNA in pharyngeal swabs and lungs; however, despite circulating neutralizing antibody available at the time of challenge, viral RNA was still detected 7 days after rechallenge. Viral RNA in pharyngeal swabs on day 5 following rechallenge and in lung tissue on day 7 could indicate that asymptomatic reinfection is possible. Prolonged viral shedding has been observed in human COVID-19 cases, with detectable neutralizing antibody titers (20). Alternatively, the RNA detected in the swabs could be input virus that is slowly being cleared from the respiratory system.

Currently, convalescent plasma is an option to treat severe cases of COVID-19 (21). Other antibody-based options include manufactured polyclonal antibodies or MAbs that represent avenues to prevent or treat SARS-CoV-2 infections as a standardized product. Several groups have reported *in vitro* characterization of anti-SARS-CoV-2-neutralizing MAbs, and a number of antibodies have been shown to protect in small animal models, including Syrian hamsters (3, 22). Here, pretreatment with MAb Centi-F1 resulted in weight maintenance throughout the experiment, lower-trending levels of viral RNA detected in pharyngeal swabs and lung tissues and, most importantly, reduced levels of infectious virus detected in the lung. The lack of statistical significance in pharyngeal swabs and lung homogenates could possibly be obviated using a subgenomic RNA assay; however, passive transfer of IgG failing to adequately protect the upper airway (23) may also play a role.

Our results expand on the earlier findings that the Syrian hamster model is a suitable small animal model of COVID-19 (2). Transient and reversible immunosuppression using CyP can be used to increase the severity and duration of the disease state. The advantages of the CyP model are that the wild-type hamsters are readily available and would produce a normal immune response to vaccination. One disadvantage is that disruption of lymphocytes could confound the evaluation of therapeutics that target components of the immune response or of vaccines that require rapid mobilization of the adaptive response. For evaluation of those types of medical countermeasures, the wild-type hamster would be preferred. This is the first report that SARS-CoV-2 is lethal in *RAG2* KO hamsters. For practical purposes, uniformly lethal models allow fewer numbers of animals be used to detect significant levels of protection, facilitating rapid screening of candidate therapeutics. *RAG2* KO hamsters would not be suitable for the

use in active vaccine studies but could be used for antibody passive transfer studies. For example, passive transfer of immune serum from nonhuman primate or human vaccine studies could be an approach to investigate mechanisms of protection. Overall, our hamster SARS-CoV-2 models with severe diseases clinically relevant to those of COVID-19 patients provide a platform for evaluating candidate medical countermeasures to combat the pandemic.

MATERIALS AND METHODS

Ethics. Animal research was conducted under an IACUC-approved protocol at USAMRIID (USDA registration number 51-F-00211728 and OLAW assurance number A3473-01) in compliance with the Animal Welfare Act and other federal statutes and regulations relating to animals and experiments involving animals. The facility where this research was conducted is fully accredited by the Association for Assessment and Accreditation of Laboratory Animal Care, International, and adheres to principles stated in the *Guide for the Care and Use of Laboratory Animals* (24).

SARS-CoV-2 stock. An aliquot of the third passage of SARS-CoV-2 USA-WA-1/2020 was received from the CDC and propagated in ATCC Vero 76 cells (99% confluent) in Eagle's minimal essential medium (EMEM) containing 1% GlutaMax, 1% nonessential amino acids (NEAA), and 10% heat-inactivated fetal bovine serum (FBS) at a multiplicity of infection (MOI) of 0.01. Supernatant was collected from cultures exhibiting a characteristic cytopathic effect (CPE) and clarified by centrifugation (10,000 $\times$ *g* for 10 min). Clarified virus was subjected to the following specifications: (i) identification by SARS-CoV-2 RT-PCR assay, (ii) quantification by agarose-based plaque assay, (iii) determination of freedom from contaminants by growth of chocolate agar plates, (iv) endotoxin testing using an Endosafe nexgen-PTS instrument, (v) mycoplasma testing using the MycoAlert test kit, and (vi) genomic sequencing. For experiments with a challenge dose of $\leq$10,000 PFU, virus p5 was used; for experiments with a challenge dose of 100,000 PFU, p6 was used. Genomic analysis indicates no changes between p3, p5, and p6 lots.

Animal procedures. Wild-type (females only, aged 6 to −8 weeks) or *RAG2* KO (females and males, aged 11 to 12 weeks) hamsters (*Mesocricetus auratus*) were anesthetized by inhalation of vaporized isoflurane using an IMPAC6 veterinary anesthesia machine for the following procedures: intranasal challenge of virus, CyP intraperitoneal injections, pharyngeal swabs, and nonterminal blood collection. Intranasal instillation of SARS-CoV-2 was administered in a volume of 50 μl for challenge doses of 100, 1,000 and 10,000 PFU, and a volume of 100 μl for the challenge dose of 100,000 PFU. CyP treatment (pharmaceutical grade; Baxter) consisted of an initial loading dose of 140 mg/kg followed by maintenance doses of 100 mg/kg on the days indicated by each experiment. Pharyngeal swabs in 0.5 ml of complete medium were used for virus detection to monitor infection and disease course in hamsters. Vena cava blood collection was limited to 7% of total blood volume per week. Terminal blood collection was performed by cardiac injection at the time of euthanasia. All work involving animals was performed in an animal biosafety level 3 (ABSL3) laboratory.

Anti-SARS-CoV-2 MAb. F01 MAb was administered to hamsters at a dose of 30 mg/kg by the subcutaneous route. F01 MAb was a kind gift from Distributed Bio, Inc.

Viral RNA assay. Following 3 freeze/thaw cycles of frozen swabs in medium, 250 μl of medium was removed and added to 750 μl of TRIzol LS. Approximately 200 mg of organ tissue was homogenized in 1.0 ml of TRIzol using M Tubes on the gentleMACS dissociator system on the RNA setting. RNA was extracted from TRIzol LS or TRIzol per the manufacturer's protocol. A NanoDrop 8000 instrument was used to determine the RNA concentration, which was then raised to 100 ng/μl in UltraPure distilled water. Samples were run in duplicate on a Bio-Rad CFX thermal cycler using a TaqPath one-step RT-qPCR mastermix according to the CDC's recommended protocol of 25°C for 2 min, 50°C for 15 min, and 95°C for 2 min, followed by 45 cycles of 95°C for 3 s and 55°C for 30 s. The forward and reverse primer and probe sequences were as follows: 2019-nCoV_N2-F, 5'-TTA CAA ACA TTG GCC GCA AA-3'; 2019-nCoV_N2-R, 5'-GCG CGA CAT TCC GAA GAA-3'; and 2019-nCoV_N2-P, 5'-ACA ATT TCC CCC AGC GCT TCA G-3'. The limit of detection for this assay is 50 copies.

PRNT. An equal volume of complete medium (cEMEM; EMEM containing 10% heat-inactivated FBS, 1% penicillin/streptomycin [Pen/Strep], 0.1% gentamycin, and 0.2% amphotericin B [Fungizone]) containing SARS-CoV-2 was combined with 2-fold serial dilutions of cEMEM containing antibody and incubated at 37°C in a 5% CO_2 incubator for 1 h (total volume, 222 μl). Aliquots (180 μl per well) of the combined virus/antibody mixture were then added to 6-well plates containing 3-day-old ATCC Vero 76 monolayers and allowed to adsorb for 1 h in a 37°C, 5% CO_2 incubator. Aliquots (3 ml per well) of agarose overlay (0.6% SeaKem ME agarose, Earl's basal medium Eagle [EBME] with HEPES, 10% heat-inactivated FBS, 100$\times$ NEAA, 1% Pen/Strep, 0.1% gentamycin, and 0.2% amphotericin B) were then added and allowed to solidify at room temperature. The plates were placed in a 37°C, 5% CO_2 incubator for 2 days and then 2 ml per well of agarose overlay containing 5% neutral red and 5% heat-inactivated FBS was added. After 1 additional day in a 37°C, 5% CO_2 incubator, plaques were visualized and counted on a light box. $PRNT_{80}$ titers are the reciprocal of the highest dilution that results in an 80% reduction in the number of plaques relative to the number of plaques visualized in the wells containing cEMEM alone (no antibody).

Plaque assay. Approximately 200 mg of lung tissue was homogenized in 1.0 ml of cEMEM using gentleMACS M Tubes and a gentleMACS dissociator on the RNA setting. Tubes were centrifuged to pellet debris, and supernatants were collected. Tenfold dilutions of the samples were adsorbed to Vero 76 monolayers (200 μl of each dilution per well). Following a 1-h adsorption in a 37°C, 5% CO_2 incubator,

cells were overlaid and stained identically as described for PRNT. The limit of detection for this assay is 50 PFU.

Hematology. Whole blood collected in EDTA tubes was analyzed on an HM5 hematology analyzer on the DOG2 setting.

Preparation of tissues for histology. Tissues were fixed in 10% neutral buffered formalin, trimmed, processed, embedded in paraffin, cut at 5 to 6 μm, and stained with hematoxylin and eosin (H&E).

***In situ* hybridization.** To detect SARS-CoV-2 genomic RNA in FFPE tissues, *in situ* hybridization (ISH) was performed using the RNAscope 2.5 high-definition (HD) Red kit (Advanced Cell Diagnostics, Newark, CA) as described previously (25). Briefly, 40 ZZ ISH probes targeting SARS-CoV-2 genomic RNA fragment 21571–25392 (GenBank accession number LC528233.1) were designed and synthesized by Advanced Cell Diagnostics (catalog no. 854841). Tissue sections were deparaffinized with xylene, underwent a series of ethanol washes and peroxidase blocking, and were then heated in kit-provided antigen retrieval buffer and digested by kit-provided proteinase. Sections were exposed to ISH target probe pairs and incubated at 40°C in a hybridization oven for 2 h. After rinsing, ISH signal was amplified using a kit-provided preamplifier and amplifier conjugated to alkaline phosphatase and incubated with a fast red substrate solution for 10 min at room temperature. Sections were then stained with hematoxylin, air dried, and cover slipped.

Immunofluorescence. Formalin-fixed paraffin-embedded (FFPE) tissue sections were deparaffinized using xylene and a series of ethanol washes. After 0.1% Sudan black B (Sigma) treatment to eliminate the autofluorescence background, the sections were heated in Tris-EDTA buffer (10 mM Tris base, 1 mM EDTA solution, and 0.05% Tween 20 [pH 9.0]) for 15 min to reverse formaldehyde cross-links. After rinses with PBS (pH 7.4), the sections were blocked with PBT (PBS plus 0.1% Tween 20) containing 5% normal goat serum overnight at 4°C. Then the sections were incubated with rabbit anti-SARS-CoV spike (1:200, catalog no. 40150-T62-COV2; Sino Biological) or mouse anti-SARS-CoV NP (1:200, catalog no. 40143-MM05; Sino Biological) antibodies and mouse anti-pan-cytokeratin (1:100, catalog no. sc-8018; Santa Cruz Biotechnology), mouse anti-CC10 (1:100, catalog no. sc-365992; Santa Cruz Biotechnology), mouse anti-E-cadherin (1:100, catalog no. 33-4000; Thermo Fisher) antibodies for 2 h at room temperature. After rinses with PBT, the sections were incubated with secondary goat anti-rabbit Alexa Fluor 488 (1:500, Thermo Fisher) and goat anti-mouse Alexa Fluor 568 (1:500, Thermo Fisher) antibodies for 1 h at room temperature. Sections were cover slipped using the Vectashield mounting medium with 4′,6-diamidino-2-phenylindole (DAPI; Vector Laboratories). Images were captured on a Zeiss LSM 880 confocal system and processed using ImageJ software.

Transmission electron microscopy. Fresh hamster lung and trachea were harvested after euthanasia and submerged in 2.5% glutaraldehyde and 2% paraformaldehyde in 0.1 M sodium phosphate buffer for 1 to 3 h and then placed in 4% paraformaldehyde for 14 or 21 days for viral inactivation. Samples were submerged in Microchem prior to removal from containment suites. Tissue was trimmed and then rinsed with 0.1 M sodium cacodylate buffer before postfixing with 1% osmium tetroxide in 0.1 M sodium cacodylate. After osmium fixation, the samples were rinsed with 0.1 M sodium cacodylate buffer, followed by a water wash, and then subjected to uranyl acetate *en bloc*. Samples were washed with water, then dehydrated through a graded ethanol series that included 3 exchanges with 100% ethanol. Samples were further dehydrated with equal volumes of 100% ethanol and propylene oxide followed by two changes of propylene oxide. Samples were initially infiltrated with equal volumes of propylene oxide and resin (Embed-812; EMS, Hatfield, PA), then incubated overnight in propylene oxide and resin. The next day, the samples were infiltrated with 100% resin, embedded and oriented in 100% resin, and then allowed to polymerize for 48 h at 60°C. Sections (1 μm thick) were cut from each tissue block, a region of interest for thin sectioning was chosen, and 80-nm thin sections were cut and collected on 200-mesh copper grids. Two grids from each sample was further contrast stained with 2% uranyl acetate and Reynold's lead citrate. Samples were then imaged on the Jeol 1011 transmission electron microscope (TEM) at various magnifications.

Statistical analyses. Statistical analyses were completed using GraphPad Prism 8. Weight data were analyzed using a one-way analysis of variance (ANOVA) with multiple comparisons for experiments with $\geq$3 groups; unpaired t tests were used to analyze weight data for experiments with 2 groups. Comparisons of lymphocyte levels and lung viral load were assessed using unpaired t tests. Significance of survival data was assessed using log rank tests. In all analyses, a P value of $<$0.05 is considered statistically significant.

Data availability. All data are available in the main text or the supplemental material.

SUPPLEMENTAL MATERIAL

Supplemental material is available online only.
SUPPLEMENTAL FILE 1, XLSX file, 0.02 MB.

ACKNOWLEDGMENTS

REFERENCES

1. Cohen J. 2020. From mice to monkeys, animals studied for coronavirus answers. Science 368:221–222. https://doi.org/10.1126/science.368.6488.221.

2. Chan JF, Zhang AJ, Yuan S, Poon VK, Chan CC, Lee AC, Chan WM, Fan Z, Tsoi HW, Wen L, Liang R, Cao J, Chen Y, Tang K, Luo C, Cai JP, Kok KH, Chu H, Chan KH, Sridhar S, Chen Z, Chen H, To KK, Yuen KY. 2020. Simulation of the clinical and pathological manifestations of coronavirus disease 2019 (COVID-19) in golden Syrian hamster model: implications for disease pathogenesis and transmissibility. Clin Infect Dis https://doi.org/10.1093/cid/ciaa325.

3. Rodgers TF, Zhao F, Huang D, Beutler N, Abbott RK, Callaghan S, Garcia E, He W, Hurtado J, Limbo O, Parren M, Peng L, Ricketts J, Ricciardi MK, Smith C, Song G, Woehl J, Yang L, Rawlings S, Smith DM, Nemazee D, Teijaro JR, Voss JE, Andrabi R, Briney B, Landais E, Sok D, Jardine JG, Burton DR. 2020. Rapid isolation of potent SARS-CoV-2 neutralizing antibodies and protection in a small animal model. bioRxiv https://doi.org/10.1101/2020.05.11.088674.

4. Schaecher SR, Stabenow J, Oberle C, Schriewer J, Buller RM, Sagartz JE, Pekosz A. 2008. An immunosuppressed Syrian golden hamster model for SARS-CoV infection. Virology 380:312–321. https://doi.org/10.1016/j.virol.2008.07.026.

5. Huang C, Wang Y, Li X, Ren L, Zhao J, Hu Y, Zhang L, Fan G, Xu J, Gu X, Cheng Z, Yu T, Xia J, Wei Y, Wu W, Xie X, Yin W, Li H, Liu M, Xiao Y, Gao H, Guo L, Xie J, Wang G, Jiang R, Gao Z, Jin Q, Wang J, Cao B. 2020. Clinical features of patients infected with 2019 novel coronavirus in Wuhan, China. Lancet 395:497–506. https://doi.org/10.1016/S0140-6736(20)30183-5.

6. Kim ES, Chin BS, Kang CK, Kim NJ, Kang YM, Choi JP, Oh DH, Kim JH, Koh B, Kim SE, Yun NR, Lee JH, Kim JY, Kim Y, Bang JH, Song KH, Kim HB, Chung KH, Oh MD, Korea National Committee for Clinical Management of C. 2020. Clinical course and outcomes of patients with severe acute respiratory syndrome coronavirus 2 infection: a preliminary report of the first 28 patients from the Korean cohort study on COVID-19. J Korean Med Sci 35:e142. https://doi.org/10.3346/jkms.2020.35.e142.

7. Tan L, Wang Q, Zhang D, Ding J, Huang Q, Tang YQ, Wang Q, Miao H. 2020. Lymphopenia predicts disease severity of COVID-19: a descriptive and predictive study. Signal Transduct Target Ther 5:33. https://doi.org/10.1038/s41392-020-0148-4.

8. Miao J, Ying B, Li R, Tollefson AE, Spencer JF, Wold WSM, Song SH, Kong IK, Toth K, Wang Y, Wang Z. 2018. Characterization of an N-terminal non-core domain of RAG1 gene disrupted Syrian hamster model generated by CRISPR Cas9. Viruses 10:243. https://doi.org/10.3390/v10050243.

9. Goldsmith CS, Tatti KM, Ksiazek TG, Rollin PE, Comer JA, Lee WW, Rota PA, Bankamp B, Bellini WJ, Zaki SR. 2004. Ultrastructural characterization of SARS coronavirus. Emerg Infect Dis 10:320–326. https://doi.org/10.3201/eid1002.030913.

10. Kim JM, Chung YS, Jo HJ, Lee NJ, Kim MS, Woo SH, Park S, Kim JW, Kim HM, Han MG. 2020. Identification of coronavirus isolated from a patient in Korea with COVID-19. Osong Public Health Res Perspect 11:3–7. https://doi.org/10.24171/j.phrp.2020.11.1.02.

11. Neuman BW, Adair BD, Yoshioka C, Quispe JD, Orca G, Kuhn P, Milligan RA, Yeager M, Buchmeier MJ. 2006. Supramolecular architecture of severe acute respiratory syndrome coronavirus revealed by electron cryomicroscopy. J Virol 80:7918–7928. https://doi.org/10.1128/JVI.00645-06.

12. Sahin A, Erdoga A, Mutla Agaoglu P, Dineri Y, Cakirci A, Senel M, Okyay R, Tasdogan A. 2020. 2019 novel coronavirus (COVID-19) outbreak: a review of the current literature. EMJO 4:1–7. https://doi.org/10.14744/ejmo.2020.12220.

13. Ward P, et al. 6 April 2020. COVID-19/SARS-CoV-2 pandemic. Faculty of Pharmaceutical Medicine Blog. https://www.fpm.org.uk/blog/covid-19-sars-cov-2-pandemic/.

14. Vardhana SA, Wolchok JD. 2020. The many faces of the anti-COVID immune response. J Exp Med 217:e20200678. https://doi.org/10.1084/jem.20200678.

15. Boudewijns R, Thibaut HJ, Katein SJF, Li R, Vergote V, Seldeslachts L, Keyzer CD, Sharma S, Jansen S, Weyenbergh JV, Ma J, Martens E, Bervoets L, Buyten TV, Jacobs S, Lui Y, Marti-Carreras J, Vanmechelen B, Wawina-Bokalanga T, Delang L, Rocha-Pereira J, Coelmont L, Chiu W, Leyssen P, Heylen E, Schols D, Wang L, CLose L, Matthijnssens J, Ranst MV, Schramm G, Laere KV, Opdenakker G, Maes P, Weynard B, Cawthorne C, Velde GV, Wang Z, Neyts J, Dallmeier K. 2020. STAT2 signaling as double-edged sword restricting viral dissemination but driving severe pneumonia in SARS-CoV-2 infected hamsters. bioRxiv https://doi.org/10.1101/2020.04.23.056838.

16. Gu J, Gong E, Zhang B, Zheng J, Gao Z, Zhong Y, Zou W, Zhan J, Wang S, Xie Z, Zhuang H, Wu B, Zhong H, Shao H, Fang W, Gao D, Pei F, Li X, He Z, Xu D, Shi X, Anderson VM, Leong AS. 2005. Multiple organ infection and the pathogenesis of SARS. J Exp Med 202:415–424. https://doi.org/10.1084/jem.20050828.

17. Min CK, Cheon S, Ha NY, Sohn KM, Kim Y, Aigerim A, Shin HM, Choi JY, Inn KS, Kim JH, Moon JY, Choi MS, Cho NH, Kim YS. 2016. Comparative and kinetic analysis of viral shedding and immunological responses in MERS patients representing a broad spectrum of disease severity. Sci Rep 6:25359. https://doi.org/10.1038/srep25359.

18. Zhang X, Tan Y, Ling Y, Lu G, Liu F, Yi Z, Jia X, Wu M, Shi B, Xu S, Chen J, Wang W, Chen B, Jiang L, Yu S, Lu J, Wang J, Xu M, Yuan Z, Zhang Q, Zhang X, Zhao G, Wang S, Chen S, Lu H. 2020. Viral and host factors related to the clinical outcome of COVID-19. Nature 583:437–440. https://doi.org/10.1038/s41586-020-2355-0.

19. Chandrashekar A, Liu J, Martinot AJ, McMahan K, Mercado NB, Peter L, Tostanoski LH, Yu J, Maliga Z, Nekorchuk M, Busman-Sahay K, Terry M, Wrijil LM, Ducat S, Martinez DR, Atyeo C, Fischinger S, Burke JS, Slein MD, Pessaint L, Van Ry A, Greenhouse J, Taylor T, Blade K, Cook A, Finneyfrock B, Brown R, Teow E, Velasco J, Zahn R, Wegmann F, Abbink P, Bondzie EA, Dagotto G, Gebre MS, He X, Jacob-Dolan C, Kordana N, Li Z, Lifton MA, Mahrokhian SH, Maxfield LF, Nityanandam R, Nkolola JP, Schmidt AG, Miller AD, Baric RS, Alter G, Sorger PK, Estes JD, et al. 2020. SARS-CoV-2 infection protects against rechallenge in rhesus macaques. Science 369:812–817. https://doi.org/10.1126/science.abc4776.

20. Wolfel R, Corman VM, Guggemos W, Seilmaier M, Zange S, Muller MA, Niemeyer D, Jones TC, Vollmar P, Rothe C, Hoelscher M, Bleicker T, Brunink S, Schneider J, Ehmann R, Zwirglmaier K, Drosten C, Wendtner C. 2020. Virological assessment of hospitalized patients with COVID-2019. Nature 581:465–469. https://doi.org/10.1038/s41586-020-2196-x.

21. Duan K, Liu B, Li C, Zhang H, Yu T, Qu J, Zhou M, Chen L, Meng S, Hu Y, Peng C, Yuan M, Huang J, Wang Z, Yu J, Gao X, Wang D, Yu X, Li L, Zhang

J, Wu X, Li B, Xu Y, Chen W, Peng Y, Hu Y, Lin L, Liu X, Huang S, Zhou Z, Zhang L, Wang Y, Zhang Z, Deng K, Xia Z, Gong Q, Zhang W, Zheng X, Liu Y, Yang H, Zhou D, Yu D, Hou J, Shi Z, Chen S, Chen Z, Zhang X, Yang X. 2020. Effectiveness of convalescent plasma therapy in severe COVID-19 patients. Proc Natl Acad Sci U S A 117:9490–9496. https://doi .org/10.1073/pnas.2004168117.

22. Ju B, Zhang Q, Ge J, Wang R, Sun J, Ge X, Yu J, Shan S, Zhou B, Song S, Tang X, Yu J, Lan J, Yuan J, Wang H, Zhao J, Zhang S, Wang Y, Shi X, Liu L, Zhao J, Wang X, Zhang Z, Zhang L. 2020. Human neutralizing anti-bodies elicited by SARS-CoV-2 infection. Nature 584:115–119. https://doi .org/10.1038/s41586-020-2380-z.

23. Hodge LM, Marinaro M, Jones HP, McGhee JR, Kiyono H, Simecka JW. 2001. Immunoglobulin A (IgA) responses and IgE-associated inflamma-tion along the respiratory tract after mucosal but not systemic immu-nization. Infect Immun 69:2328–2338. https://doi.org/10.1128/IAI.69.4 .2328-2338.2001.

24. National Research Council. 2011. Guide for the care and use of labora-tory animals, 8th ed. National Academies Press, Washington, DC.

25. Liu J, Babka AM, Kearney BJ, Radoshitzky SR, Kuhn JH, Zeng X. 2020. Molecular detection of SARS-CoV-2 in formalin fixed paraffin embed-ded specimens. JCI Insight 5:e139042. https://doi.org/10.1172/jci .insight.139042.